ADVANCED ENERGY & SUSTAINABILITY RESEARCH
www.advenergysustres.com

Sulfur-Enhanced Performance and Durability of $SrFe_{0.75}Mo_{0.25}O_{3-\delta}/Ce_{0.9}Gd_{0.1}O_{2-\delta}$ Fuel Electrodes for Solid Oxide Fuel Cell

Matthias Riegraf, Noriko Sata, Katherine Develos-Bagarinao, and Rémi Costa*

Solid oxide fuel cells (SOFCs) are a key technology for highly efficient, low-emission power generation from hydrogen and hydrocarbon-based fuels. However, conventional Ni-cermet fuel electrodes show high performance and stability but exhibit poor tolerance toward impurities, particularly sulfur. Here, the performance and durability of Ni-free perovskite-based $SrFe_{0.75}Mo_{0.25}O_{3-\delta}$ (SFM)/$Ce_{0.9}Gd_{0.1}O_{2-\delta}$ (CGO) composite fuel electrodes are evaluated under hydrogen-rich conditions, with and without trace hydrogen sulfide in the fuel. Electrolyte-supported cells with SFM/CGO show initial performance comparable to that of benchmark Ni/CGO electrodes at 800 °C. Despite similar ohmic resistance, cells with SFM/CGO exhibit higher polarization resistance, suggesting slightly reduced electro-catalytic activity. Durability testing reveals significant degradation of SFM/CGO over time, attributed to SFM phase decomposition in hydrogen-rich atmospheres and microstructural reorganization based on post-test analysis. Surprisingly, the addition of ppm-level H_2S not only mitigated degradation, but also improved electrode performance. These results uncover a counterintuitive, sulfur-mediated stabilization mechanism for SFM-based electrodes, offering a new development pathway toward sulfur-tolerant, nickel-free SOFCs for robust and fuel-flexible energy conversion.

1. Introduction

Hydrogen is widely regarded as a key energy carrier in the decarbonization of the global energy system, offering a clean, flexible vector for decarbonizing power, industry, and transport. Realizing this potential demands rapid scale-up of electrochemical technologies, including fuel cells and electrolyzers. Among these, solid oxide cells (SOCs) stand out with their unique ability to operate reversibly in both fuel cell and electrolysis mode with unrivaled electrical efficiencies and fuel flexibility. However, despite their advantages, SOC deployment has lagged behind the low-temperature polymer exchange membrane (PEM) based technologies primarily due to higher capital expenditures (CAPEX), amongst others, associated with high system component costs.

State-of-the-art fuel electrodes for solid oxide fuel cells (SOFCs) are typically Ni-based cermets such as Ni/yttria-stabilized zirconia (YSZ) and $Ni/Ce_{0.9}Gd_{0.1}O_{2-\delta}$ (CGO). These electrodes exhibit excellent electrochemical activity for hydrogen oxidation, the water-gas shift reaction, and steam reforming of hydrocarbons, largely due to the presence of the Ni phase.[1] However, Ni-based cermets have limitations, including low-sulfur tolerance when operated with reformed natural gas or biogas,[2,3] susceptibility to carbon formation,[4,5] and poor redox stability due to the dimensional expansion of Ni upon reoxidation.[6]

The development of alternative fuel electrodes with improved characteristics could enhance flexibility in SOFC operation, simplifying system designs by eliminating the need for desulfurization units, external reformers, and reducing gas purging systems, potentially lowering overall system costs. However, identifying suitable candidates is challenging, as ideal materials must possess high ionic and electronic conductivity, electrocatalytic activity, and thermal and chemical stability under reducing conditions.

Perovskite-based materials with desirable mixed ionic and electronic conductivity (MIEC) properties and superior dimensional stability in dual atmospheres have shown promise as alternative fuel electrodes.[7] Iron molybdate double perovskites with the formula $Sr_2Fe_{1-x}Mo_xO_{6-\delta}$[8] have attracted particular research interest. They have a modified perovskite structure where the FeO_6 and MoO_6 octahedra on the B site are ordered,a resulting in high electronic conductivities, reaching up to 300 S cm^{-1} for $Sr_2FeMoO_{6-\delta}$.[9] The Mo^{6+}/Mo^{5+} and Fe^{4+}/Fe^{3+} pairs contribute to the materials' unique superlattice structure. However,

M. Riegraf, N. Sata, R. Costa
German Aerospace Centre (DLR)
Institute of Engineering Thermodynamics
Pfaffenwaldring 38-40, 70569 Stuttgart, Germany
E-mail: Matthias.Riegraf@dlr.de

K. Develos-Bagarinao
Global Zero Emission Research Center
National Institute of Advanced Industrial Science and Technology
Tsukuba, Ibaraki 305-8569, Japan

The ORCID identification number(s) for the author(s) of this article can be found under https://doi.org/10.1002/aesr.202500361.

DOI: 10.1002/aesr.202500361

$Sr_2FeMoO_{6-\delta}$ is not stable in air since the Mo solubility limit in $Sr_2Fe_{2-x}Mo_xO_{6-y}$ in air has been suggested as $x = 0.68$.[10] Therefore, most electrochemical studies have focused on $Sr_2Fe_{1.5}Mo_{0.5}O_{6-\delta}$ (SFM) to achieve high stability during redox cycling and manufacturing. SFM is often referred to as a double perovskite,[8] but is also frequently described as $SrFe_{0.75}Mo_{0.25}O_{3-\delta}$ due to the random distribution of the iron and molybdenum atoms on the B site.[8,11,12] It is reported that the disorder leads to a significantly reduced electronic conductivity in a reducing atmosphere in comparison to the compounds with a Fe/Mo ratio close to 1.[9] However, SFM is stable in air and therefore, can even be used as a high-performing symmetrical electrode.[13] Its electrical conductivity in reducing atmosphere is typically in the range 10–40 $S \cdot cm^{-1}$.[8,9,14–17] Therefore, SFM represents a highly promising material for the development of a Ni-free ceramic fuel electrode with sufficiently high electronic conductivity. In addition, SFM has been reported to enable electrochemical oxidative coupling of methane in SOCs with a high selectivity toward ethylene,[18,19] and, hence could be a promising electrode for using SOCs to produce "green" ethylene from synthetic methane. Although SFM possesses MIEC and works well as a single-phase fuel electrode,[13,20] oxygen exchange rate and hydrogen dissociation kinetics were suggested to be limited.[21–23] Therefore, SFM is often used in composite electrodes with CGO to reduce the polarization resistance.[15,24–26] Although promising results have been obtained from small-scale ($\approx$1 cm^2) SOFCs with SFM-based fuel electrodes, a reliable benchmarking against state-of-the-art cells with larger cell sizes is still lacking. Moreover, durability data for SFM-based fuel electrodes remain scarce, with most studies limited to short-term testing and lacking systematic evaluation of stability over extended operation (>500 h). Some studies have reported performance drops when sulfur impurities in the range of 100–1000 ppm were introduced to SFM-based fuel electrodes.[12,27,28] However, these studies were limited to short sulfur exposure times, leaving the long-term stability of SFM electrodes in sulfur-containing atmospheres unclear. Furthermore, no investigations have addressed lower sulfur concentrations in the 1–20 ppm range, which are representative of typical sulfur levels in the European natural gas grid.[29] A recent computational study suggested that sulfur-SFM interactions may differ at sulfur concentrations below 100 ppm, indicating that this low-sulfur regime exhibits distinct behavior.[30]

In this study, 5×5 cm^2-sized electrolyte-supported cells (ESCs) with SFM/CGO composite electrodes are investigated in SOFC operation. The primary goal is to assess the performance and durability of the electrodes in comparison with state-of-the-art Ni/CGO electrodes. Furthermore, the performance and durability of SFM/CGO fuel electrodes exposed to hydrogen sulfide is explored.

2. Results and Discussion

2.1. Crystallographic Powder Analysis

An X-ray diffraction (XRD) analysis of SFM/CGO powder mixture calcined in air at 1100 °C was carried out to investigate chemical compatibility and the pattern is displayed in **Figure 1**a. Both perovskite SFM and fluorite CGO10 phases were identified in the SFM/CGO mixture and no indications for secondary phase formations were observed. In scanning electron microscopy (SEM) images with Z contrast of the annealed SFM/CGO powder, SFM and CGO10 are identified in dark and bright particles, whose sizes range between 0.5–1 µm and 0.1–0.2 µm, respectively (Figure 1b).

For a more detailed understanding of the SFM stability in reducing atmosphere, TPR measurements of SFM and SFM/CGO powder samples were carried out in 5% H_2/Ar (see **Figure 2**). In addition, SFM/CGO powder samples were characterized via XRD after reducing the samples for 2 h in pure hydrogen at different temperatures (see **Figure 3**a,b, full range in Figure S3 and S4, Supporting Information). Subsequently, Rietveld refinements were performed for phase quantification (**Table 1**). Refined phases and molar ratios are summarized in **Table** 1 and **2**, respectively. Lattice and statistical parameters as well as Fe crystallite sizes are given in Table S1, Supporting Information and refined profiles of SFM/CGO10 powders as/calcined, reduced at 600 and 800 °C are given in Figure S1, Supporting Information, as examples. In the TPR measurements, both the SFM and the SFM/CGO samples showed pronounced peaks at ≈440 and 480 °C which are suggested to correspond to the partial reduction of Fe and Mo.[31] This was confirmed by XRD analysis of the powder reduced at 450 °C that displayed a shift of the SFM to lower angles, which corresponds to a lattice expansion suggesting a higher oxygen nonstoichiometry (Figure 3b). The TPR signal remained above the base line at temperatures >550 °C, which suggests consumption of hydrogen and is presumably due to further reduction of the SFM. Below 700 °C, SFM and CGO10 were the only identified phases and the lattice parameter of SFM was nearly

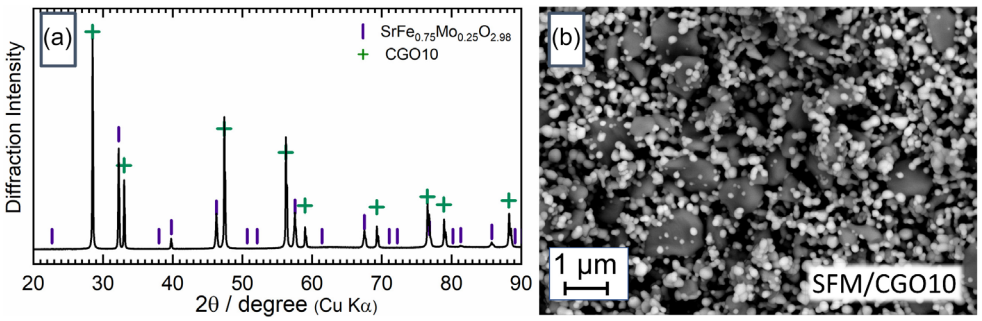

Figure 1. a) XRD pattern of the SFM/CGO powder and b) SEM image of the SFM/CGO powder. All samples were calcined at 1100 °C for 1 h in air.

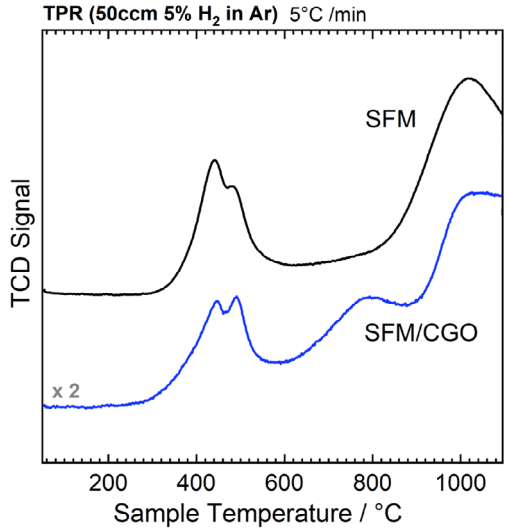

Figure 2. TPR of SFM and SFM/CGO powders in 5% H_2–Ar (50 sccm) up to 1100 °C at 5 °C min^{-1}.

unchanged between 450 and 670 °C except for 600 °C. As shown in Figure S2, Supporting Information, such a non-monotonic change of lattice parameter was not observed in pure SFM. It is possible that the CGO phase plays a role in the non-monotonic change in lattice parameter without an apparent chemical reaction between SFM and CGO; however, the origin of the small lattice parameter of SFM at 600 °C is unclear. Further detailed investigations by means of, for instance, X-ray photoelectron spectroscopy (XPS) will be needed to clarify the origin of the lattice parameter change at 600 °C, which is considered beyond the scope of the present work.

Reduction of SFM/CGO at 740 °C resulted in a further increase of the SFM lattice parameter and 5.7 mol% Fe phase formation (Figure 3c and Table 2). The SFM lattice parameter change above 700 °C could be explained by the change in Fe/Mo ratio due to extensive Fe exsolution (Figure 3d), noting that the lattice parameter increases with Mo content in SFM due to its larger cation radius.

At temperatures above ≈800 °C, the TPR profile of the SFM samples increased with a peak at ≈1000 °C indicating severe reduction. The SFM/CGO powder showed a similar behavior and displayed an additional peak at 800 °C. Pure CGO demonstrates a broad peak around 750 °C in the TPR profile, attributed to Ce^{4+} reduction.[32] SFM/CGO showed no detectable CGO10 lattice parameter change up to 860 °C by XRD, although minor reduced $CeO_{1.8}$ formation was indicated in the powder reduced at 860 °C, whose lattice parameter was 1.9%larger than that of CGO. These results suggest that Ce^{4+} reduction was confined to the particle surface at 860 °C in pure H_2, leading to negligible bulk lattice change. On the other hand, following TPR at 1100 °C in 5% H_2, the CGO lattice parameter was increased by ≈0.1% demonstrating partial reduction of Ce^{4+} of the whole CGO particles. The difference in reducing behaviors could be explained by the difference in H_2 partial pressure and temperature. At the peak temperature of 800 °C, the decomposition was even more severe with a decrease of the SFM phase to 6.3% and an increase of the Fe phase to 16.4%. Moreover, the Ruddlesden–Popper (R–P) phases (general formula $A_{n+1}B_nO_{3n+1}$, here with $n = 2$, 3) $Sr_2(MoFe)O_4$ and $Sr_3(MoFe)_2O_7$ were identified, suggesting the following decomposition reactions

$$3\,SrFe_{0.75}Mo_{0.25}O_{3-\delta} + 2H_2 \rightleftharpoons Sr_3Fe_{1.25+x}Mo_{0.75-x}O_{7-\delta} + Fe_{1-x}Mo_x + 2\,H_2O \quad (1)$$

$$2\,SrFe_{0.75}Mo_{0.25}O_{3-\delta} + 2\,H_2 \rightleftharpoons Sr_2Fe_{0.5+y}Mo_{0.5-y}O_{4-\delta} + Fe_{1-y}Mo_y + 2\,H_2O \quad (2)$$

The lattice parameter of the Fe phase ranged from 2.875 to 2.8726 Å determined by the Rietveld refinement with a body-centered cubic structure (Space group: Im-3m (229)) and was remarkably larger than that of pure Fe (2.867 Å), indicating metallic Fe alloying with Mo which is possible at 800 °C for up to ≈4 mol% Mo.[33] Thus, Equation (1) and (2) are formulated in a more general way with the formation of $Fe_{1-x}Mo_x$ alloys. On the other hand, the limited Mo content in the exsolved Fe supports the change of Fe/Mo ratio in the SFM phase due to increased Fe loss from the perovskite phase.

A further reduction of the SFM and SFM-derived R–P phase would be responsible for the wide peak at ≈1000 °C, and the fact that the Sr_2CeO_4 phase was identified when annealed above 800 °C suggests the reactions

$$2/3\,Sr_3Fe_{1.25+x}Mo_{0.75-x}O_{7-\delta} + CeO_2 + 2\,H_2 \rightleftharpoons Sr_2CeO_4 + 2/3\,Fe_{1.25+x}Mo_{0.75-x} + 2\,H_2O \quad (3)$$

$$Sr_2Fe_{0.5+y}Mo_{0.5-y}O_{4-\delta} + CeO_2 + 2\,H_2 \rightleftharpoons Sr_2CeO_4 + Fe_{0.5+y}Mo_{0.5-y} + 2\,H_2O \quad (4)$$

SFM powder reduction at different temperatures is given in Table S2 and S3, Supporting Information. After reduction at 860 °C, the original SFM phase was decreased to 5.6 mol% and exsolved Fe was increased to over 50 mol%, demonstrating significant decomposition of SFM into Fe and R–P phases. Interestingly, there are clear differences in lattice parameter evolution of SFM and Fe and crystallite size growth of Fe with reduction temperature between SFM/CGO10 and SFM powders. Apparently, Fe exsolution starts as low as 600 °C in pure SFM powder, which is much lower than 740 °C of SFM/CGO10 and the acrystallite size is about twice as larger as that in SFM/CGO10 mixture. While CGO10 phase itself has no change up to 800 °C, it might play a substantial role in the SFM chemical stability under reducing atmospheres.

With regards to literature reports about the thermo-chemical stability of SFM in reducing conditions, large discrepancies can be observed. Different studies have reported a high stability in hydrogen at temperatures higher than 1000 °C.[11–13,34,35] However, in other studies, SFM partially decomposed to metallic Fe in reducing conditions at temperatures as low as 800 °C.[9,36,37] Gou et al. observed that the main perovskite lattice remained intact, although small amounts of metallic Fe formed after 24 h in pure H_2 at 850 °C. They suggested that the metallic Fe formed when the Fe–O–Fe was broken. At 900 °C, they observed the full decomposition of the perovskite and the formation of a Sr_2MoO_4 R–P structure. Similarly, Miao et al. observed the precipitation of minor amounts of Fe of SFM after reduction in H_2

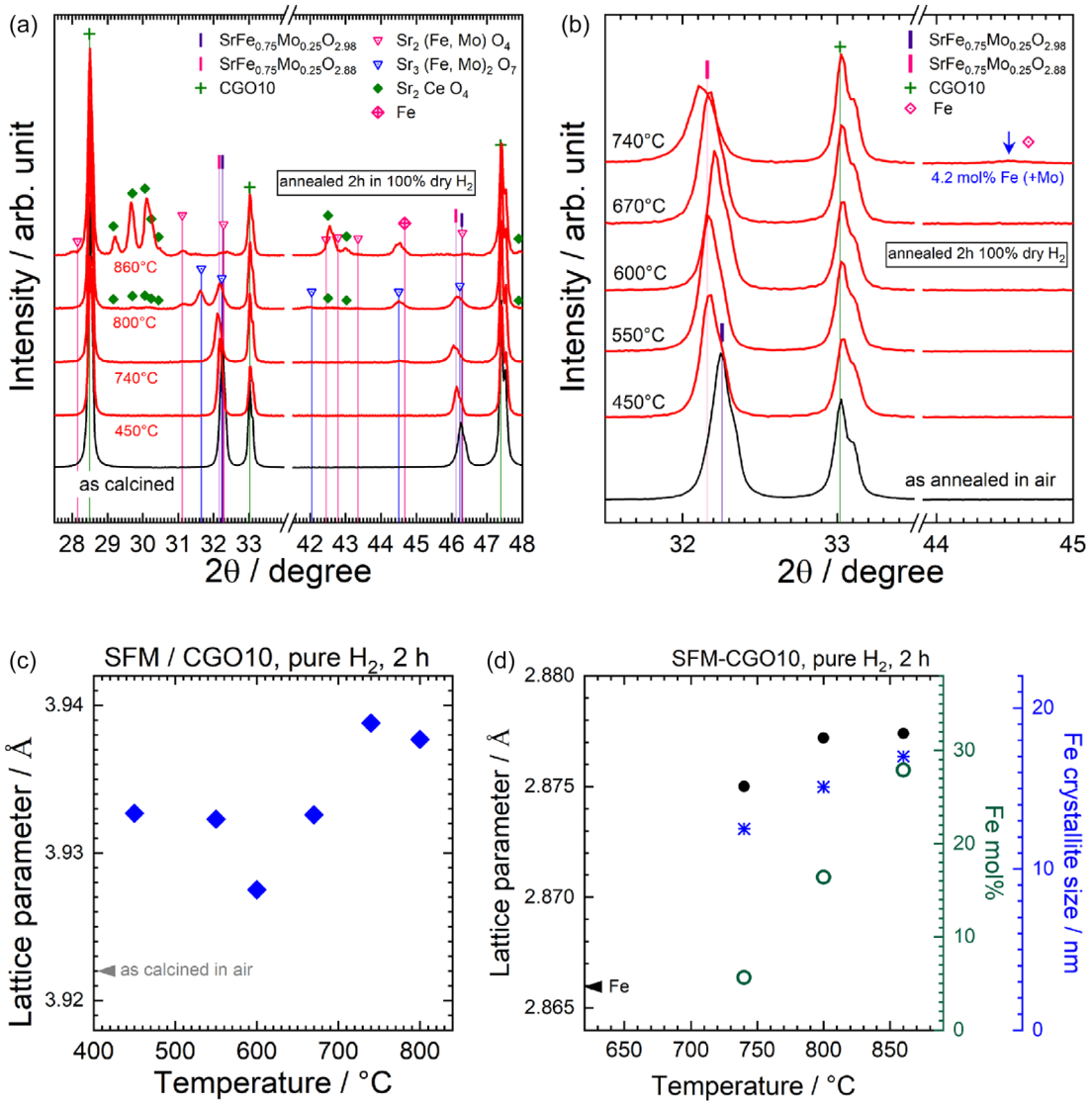

Figure 3. a,b) XRD patterns of the as-calcined SFM/CGO powder and the powder reduced in pure hydrogen for 2 h at different temperatures. c) Lattice parameter as a function of temperature determined by the Rietveld refinement. d) Refined parameters of Fe (closed and open circles, * are lattice parameter, mol% and crystallite size, respectively.

Table 1. Identified phases and their structures used in the Rietveld refinement.

Phase	Symmetry	Space group	PDF #
SFM	Cubic	Pm-3m	04-018-3456
CGO10	Cubic	Fm-3m	04-013-9775
$CeO_{1.8}$	Cubic	Fm-3m	04-003-6949
Fe(Mo)	Cubic	Im-3m	04-018-7457
$Sr_3(Mo,Fe)_2O_7$	Tetragonal	I4/mmm	04-011-8337
$Sr_2(Mo,Fe)O_4$	Tetragonal	I4/mmm	04-011-9233
Sr_2CeO_4	Orthorhombic	Pbam	04-014-6763
$SrCeO_3$	Orthorhombic	Pnma	04-006-1683

for 10 h at 800 °C.[9] Xiao et al. observed a reduction of Fe^{2+} to Fe^0 at temperatures above 800 °C.[37]

Differences in microstructure, such as grain size, as well as the synthesis route (e.g., solid-state versus sol-gel methods), can strongly influence phase stability and segregation behavior of perovskites under reducing conditions.[38] Such factors likely contribute to the discrepancies observed among reported values in the literature. Nevertheless, the reasons for the reported discrepancies remain unclear.

2.2. SFM/CGO Electrode Treatment in Hydrogen

A processing temperature of 1100 °C for a pure SFM electrode was identified to lead to good necking between SFM particles

Table 2. Molar percentages of the SFM/CGO powder samples reduced at different temperatures in pure hydrogen for 2 h and powder sample after TPR measurement, determined by Rietveld refinement (50:50 vol. ratio of SFM/CGO equals to 40:60 in mol%).

Molar %	As-calcined	450 °C	550 °C	600 °C	670 °C	740 °C	800 °C	860 °C	TPR [5% H_2, max 1100 °C]
SFM	45.0	43.0	42.3	42.2	41.4	31.6	6.29		
CGO10	55.0	57.0	57.7	57.8	58.6	62.8	62.3	45.8	53.5
$CeO_{1.8}$								0.5	
Fe(Mo)						5.7	16.4	27.9	19.2
$Sr_3(Mo,Fe)_2O_7$							8.9	1.6	2.1
$Sr_2(Mo,Fe)O_4$							4.4	1.4	24.3
Sr_2CeO_4							1.7	22.8	
$SrCeO_3$									0.9

and a fine microstructure (Figure S5, Supporting Information). Dilatometry measurements of SFM showed a CTE of overall $16.8{\cdot}10^{-6}\,K^{-1}$ in the range 100–1190 °C (Figure S6, Supporting Information), consistent with previous literature studies.[8,12,16,39,40] Since the CGO in the interlayer of the substrate has a significantly lower CTE value of $\alpha_{CGO} = 12.7{\cdot}10^{-6}\,K^{-1}$,[41] the CTE mismatch at the CGO|SFM interface was likely too large, which led to a delamination of pure SFM electrodes after annealing due to large residual thermal stresses (Figure S6, Supporting Information). By contrast, SFM/CGO composite electrodes showed good adhesion to the CGO interlayer after sintering at 1100 °C, most likely due to the reduction of the electrode layer's apparent CTE and its alignment to the CGO interlayer. After annealing, a fuel electrode thickness of ≈15 µm was obtained (**Figure 4**a).

After reducing a half cell consisting of the electrolyte, interlayer, and fuel electrode for 2 h at 800 °C in pure hydrogen, this sample and a nonreduced reference sample were investigated using NanoSIMS analysis, which allows for chemical imaging of large volumes with a high spatial resolution down to 50 nm (see Figure 4).

The as-prepared SFM/CGO electrode in Figure 4c–e shows two clearly separated phases. The blue color corresponding to the Ce signal indicates the presence of the CGO phase. The yellow color is obtained by mixing the Sr (in green) and Fe (in red) signals and shows a homogeneous composition of the initial SFM phase.

By contrast, the SIMS image of the reduced SFM/CGO electrode in Figure 4g,h depicts a number of other colors indicating the presence of additional phases in the electrode. Whereas the blue CGO phase is still present in a large amount, the area of the yellow SFM phase in the cross-section has significantly decreased, indicating its decomposition in agreement with the SFM/CGO powder experiments in the previous section. No clear trend in color differences could be observed between the particle surfaces and their interior, demonstrating the progression of the SFM decomposition into the bulk.

In addition, light blue regions can be identified throughout the entire electrode due to an overlap of the Ce (blue) and the Sr (green) signals, consistent with the observed formation of 2 mol% Sr_2CeO_4 in the SFM/CGO powder reduced at 800 °C (see Figure 4 and Table 1). Furthermore, red regions are visible in the reduced electrode, suggesting the formation of elemental iron. Purple regions are also abundant throughout the electrode indicating the overlap of Fe and Ce. However, since no Fe–Ce species were identified in the XRD analysis of the reduced SFM/CGO powder, it is likely that the purple region rather indicate small Fe particles that diffused into the porous CGO structure. These Fe particles are also present in the CGO interlayer, indicating their high mobility after formation. Furthermore, green areas can be detected in the NanoSIMS images, indicating Sr-enrichment which could potentially be associated with the formation of the R–P phases observed in Figure 4.

2.3. Electrochemical Performance

Initial SOFC performance at 800 °C was assessed by means of current-voltage characteristics (*i-V* curve) and electrochemical impedance spectroscopy. A comparison between ESC with a state-of-the-art Ni/CGO fuel electrode and with SFM/CGO electrode was carried out by investigating multiple cells of both cell types and the mean performance values are given in **Table 3**. SEM images of the ESCs with Ni/CGO fuel electrode are shown elsewhere,[42,43] and show initial particle sizes of 0.5–1 µm for Ni, and 0.1–0.2 µm for CGO. The electrochemical behavior of a representative cell of each type is depicted in **Figure 5**.

The average current density of eight different SFM/CGO-based ESC of nominally equal composition at 0.6 V was $0.62\,A\,cm^{-2}$, which was slightly lower than the $0.68\,A\,cm^{-2}$ obtained for the Ni/CGO-based cells ($n = 2$). Corresponding power densities at 0.6 V were 0.37 and $0.4\,W\,cm^{-2}$, respectively. Both ohmic and polarization resistance were slightly higher for the cells with SFM/CGO fuel electrode. Nevertheless, the difference in ohmic resistance was within one standard deviation. Two of the eight investigated SFM/CGO-based cells showed a significantly decreased performance, which was mainly caused by an increased ohmic resistance and likely related to poor contacting of the cells (see Figure S7, Supporting Information). Upon the exclusion of these cells, the average performance of the remaining six cells was $0.65\,A\,cm^{-2}$ and thus, closer to those of the state-of-the-art cells. In this case, the same average ohmic resistance values were obtained. In our recent investigation of Ni-doped lanthanum strontium chromite fuel electrodes with an estimated electronic conductivity of ≈1 $S\,cm^{-1}$, we observed an increased

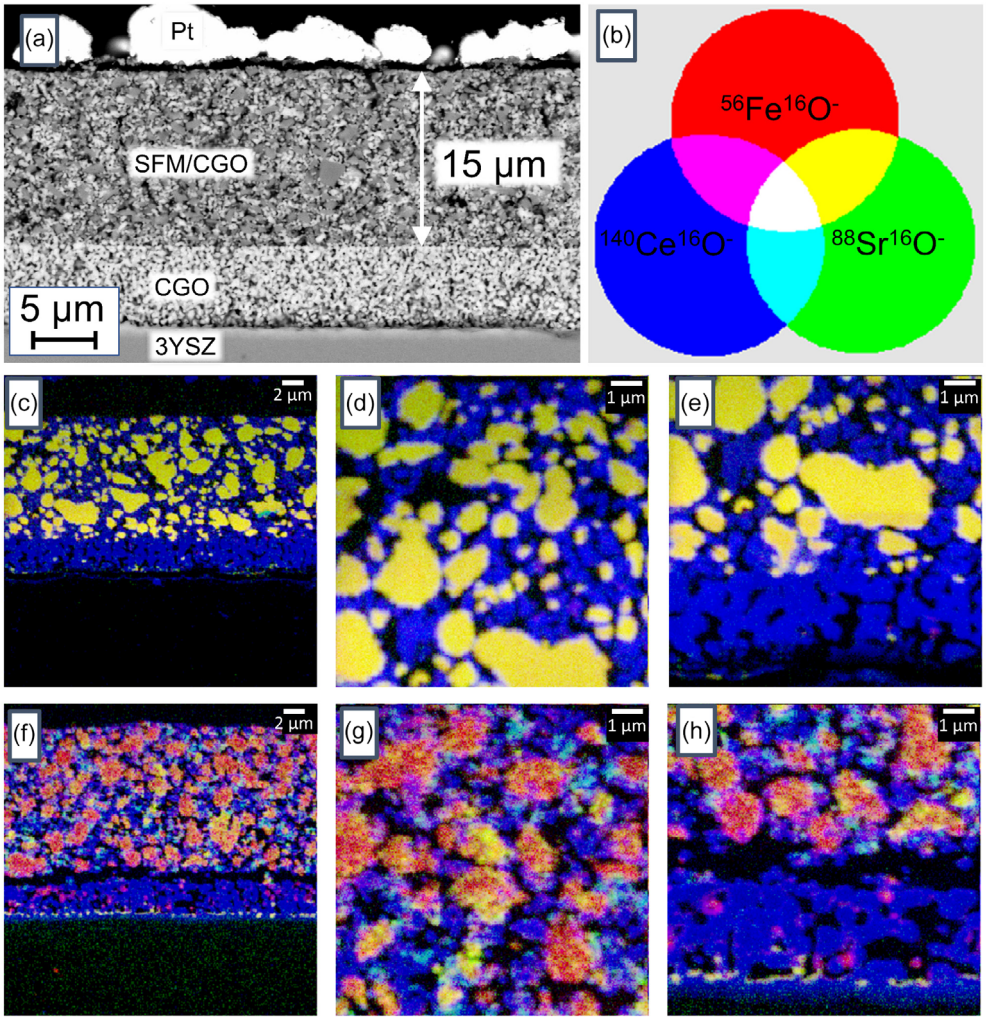

Figure 4. a) SEM image of the polished sample of the as-produced SFM/CGO fuel electrode, b) RGB composition overlay of the analyzed secondary ion intensities of $^{56}Fe^{16}O^-$, $^{88}Sr^{16}O^-$, and $^{140}Ce^{16}O^-$. c–h) SIMS elemental mapping depicting their distribution at the region of interest comprising the SFM/CGO fuel electrode (c–e) as-prepared and (f–h) reduced in pure hydrogen at 800 °C for 2 h. c,f: 30 µm raster size; d,e,g,h: 10 µm raster size.

Table 3. Sample size, and average values and standard deviation of current density and power density at 0.6 V, ohmic resistance and polarization resistance for the different cell types.

	Sample size n [–]	Current density i @ 0.6 V [A cm^{-2}]	Power density @ 0.6 V [W cm^{-2}]	Ohmic resistance R_{ohm} @ OCV [Ω cm^2]	Polarization resistance R_{pol} @ OCV [Ω cm^2]
Ni/CGO	2	0.68 ± 0.01	0.4 ± 0.01	0.64 ± 0.00	0.14 ± 0.00
SFM/CGO-all	8	0.62 ± 0.06	0.37 ± 0.04	0.67 ± 0.06	0.19 ± 0.03
SFM/CGO-high performance	6	0.65 ± 0.01	0.39 ± 0.01	0.64 ± 0.02	0.18 ± 0.01

ohmic resistance compared to cells with Ni/CGO fuel electrodes and suggested that the performance of SOFC with alternative fuel electrodes could be improved by employing perovskites with higher electronic conductivity.[43] By contrast, in the present study, current collection and electronic conductivity seem to be high enough that they do not limit the performance for the SFM/CGO fuel electrodes since the ohmic resistances of SFM/CGO and Ni/CGO-based ESC are approximately the same. Hence, the electrochemically active thickness can be assumed to be lower than the electrode thickness and the influence of the Pt layer on the electrochemical performance is negligible. Furthermore, initial particle size of the brushed Pt particles was in the range of 5 µm (Figure 3a) significantly lower than the electrode particles. As a result, the triple phase boundary length contribution between ionic conductor (SFM + CGO)|Pt| gas phase was assumed to be low. Nevertheless, the polarization

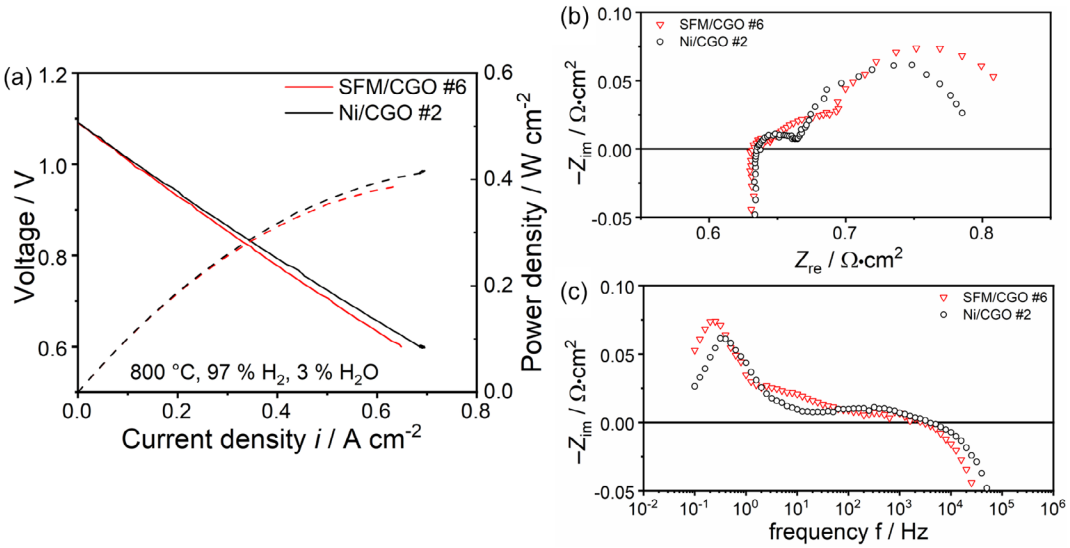

Figure 5. a) *i–V* curves of the tested cells at 800 °C and in 97% H_2, 3% H_2O fuel gas. b,c) Nyquist and imaginary impedance plots of the cells at OCV during the initial characterization.

resistance of the cells with SFM/CGO was still increased compared to state-of-the-art cells (0.18 Ω cm^2 vs. 0.14 Ω cm^2). The state-of-the-art ESC employed an $La_{0.6}Sr_{0.4}Co_{0.2}Fe_{0.8}O_{3-\delta}$ (LSCF)/CGO functional oxygen electrode, whereas the SFM/CGO-based cell had a pure LSCF electrode. Since performance contributions of LSCF-based oxygen electrodes to overall performance was shown to be small in state-of-the-art ESC at temperatures above 800 °C,[44] their impact on cell performance was assumed to be negligible. Thus, the difference in impedance response at 10 and 0.1 Hz (Figure S7c, Supporting Information) is likely related to the fuel electrode.[15]

2.4. Degradation Behavior with and Without Sulfur Addition

As a next step, the performance and durability of SFM/CGO-based cells with and without the addition of H_2S in the fuel gas were investigated at 800 °C and 0.375 A cm^{-2} for a preliminary assessment of the electrode's electrochemical characteristics in a system without desulfurization unit. The evolution of the cell voltages over time periods of 600–700 h during two test campaigns in the 4-cell test rig is depicted in **Figure 6**. Three of the six tested cells were exposed to 1, 5, and 20 ppm H_2S, respectively, whereas the other three cells were operated without the addition of sulfur. For the sulfur-exposed cells with 1, 5, and 20 ppm H_2S, the cell voltage increased within 30 mins after sulfur addition by 3, 4, and 8 mV, respectively (Figure 6c). This activation behavior was associated with a decrease of the polarization resistance in the time period between $t = 21$ and 90 h, which is illustrated for the impedance spectra of the cell exposed to 20 ppm H_2S in **Figure 7**a,b. The addition of sulfur led to a decrease of the low-frequency arc at frequencies from 0.1 to 10 Hz, suggesting the presence of one or more fuel electrode surface processes in this frequency region in accordance with literature studies of SFM/CGO electrodes.[15] The low frequency of the process indicates the occurrence of a chemical capacitance similar to other MIECs.[45] In such cases, a double layer occurs at the MIEC surface due to adsorbed ions and accumulated electronic charges in the space-charge layer.[46] A change in operating conditions (e.g., potential, temperature, gas phase composition) in such MIEC electrodes is frequently associated with a change in oxygen nonstoichiometry.

In our previous studies, we carried out analogous sulfur poisoning tests for Ni/YSZ, Ni/CGO, and L65SCrN fuel electrodes and extensively discussed the issue of sulfur poisoning of Ni-containing electrodes.[2,3,43] After addition of 20 ppm H_2S, Ni/YSZ-based cells showed pronounced voltage drops of more than 150 mV at 850 °C and 0.5 A cm^{-2}. While the voltage drops were only 35 mV and 10 mV for L65SCrN (860 °C) and Ni/CGO electrodes (850 °C), respectively, voltage drops were observed in all cases. In all our previous investigations, sulfur poisoning solely caused an increase of the polarization resistance since it led to blockage of the electro-catalytically active Ni surfaces. Accordingly, the decrease of polarization resistance in the present study suggests a kinetic-enhancing effect of sulfur on the SFM-based electrodes.

After the initial poisoning, the durability behavior of all cells was investigated. In Figure 6a, the cell without sulfur showed a voltage decrease of 32 mV in the time between $t = 22$ h and 595 h ($\Delta t = 573$ h), whereas the cell exposed to 20 ppm hydrogen sulfide only decreased by 12 mV. In Figure 6b, the cell voltage of the cell exposed to 5 ppm decreased by 32 mV in the time between $t = 2$ and 652 h ($\Delta t = 650$ h), that of the 1 ppm cell by 35 mV, and those of the cells operated in the absence of sulfur by 63 mV (cell #5) and 45 mV (cell #3), respectively. Hence, a clear decrease in the degradation rate can be observed when the SFM/CGO electrodes were exposed to hydrogen sulfide.

For more detailed analysis, degradation was monitored by electrochemical impedance spectroscopy (EIS) and representative results of the first test campaign are shown in Figure 7a–d. Results of the second campaign are depicted in Figure S8, Supporting

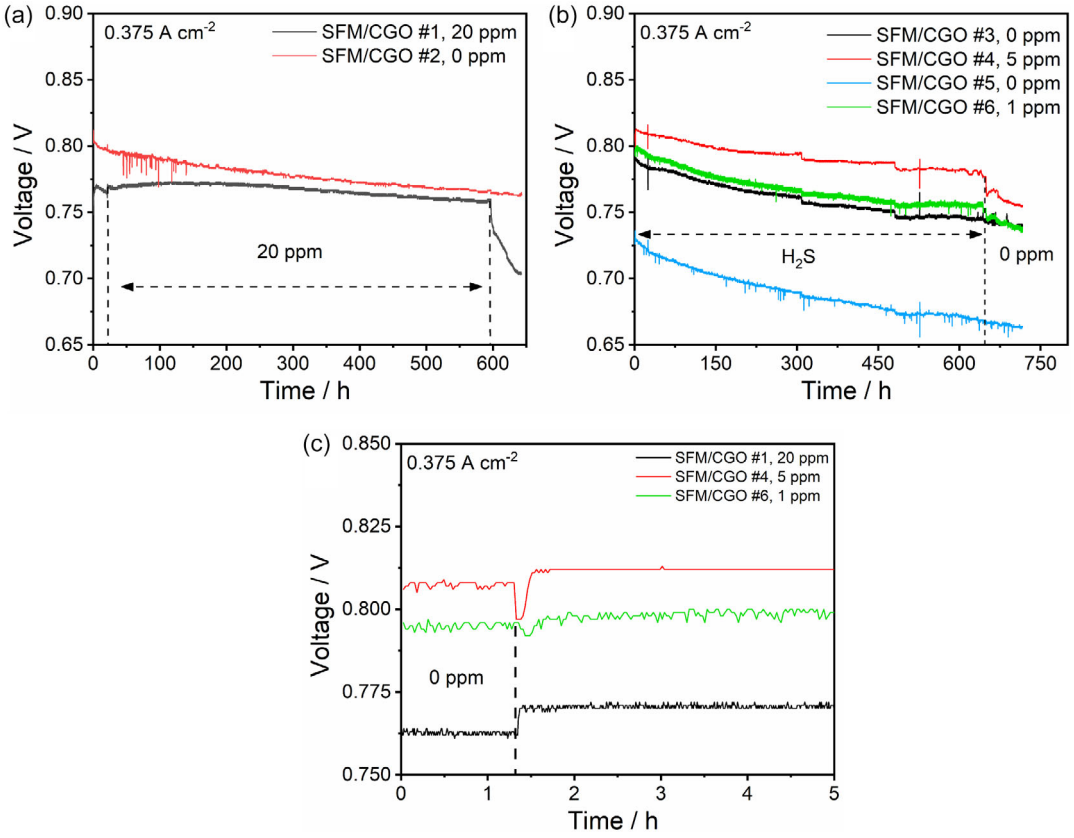

Figure 6. Durability tests of SFM/CGO-based cells at 800 °C, 97% H_2, 3% H_2O, and 0.375 A cm^{-2} with a) 0 (SFM/CGO #2) and 20 ppm H_2S(SFM/CGO #1) over 644 h, b) 0 (SFM/CGO #3 and SFM/CGO #5), 5 ppm H_2S(SFM/CGO #4) and 1 ppm H_2S(SFM/CGO #6) over 670 h. c) Short-term sulfur poisoning tests for the cells with 1, 5 and 20 ppm H_2S. The cell voltages in Figure b) show two kinks at 300 and 500 h which were related to the depletion of water in the bubbler. After refilling, the voltages recovered.

Information. Based on these data, the changes of the ohmic and the polarization resistance after 500 h of durability testing were derived and are summarized in Figure 7e. The results show a statistically significant decreased in degradation of both the ohmic and the polarization resistance for the cell operated with 5 ppm H_2S of more than one standard deviation compared to the average values of the sulfur-free cells. The change of both resistances was even less for the cell exposed to 20 ppm H_2S. The polarization resistance of all cells in the present study showed a similar increase in the frequency region of ≈100 Hz which was not affected by the exposure to sulfur. Thus, the process is most likely related to an SFM/CGO electrode bulk process, such as the oxygen ion migration across the SFM|CGO interface. In addition, all sulfur-free cells displayed a considerable increase in polarization resistance over time in the frequency range between 0.1 and 5 Hz. However, this degradation process was substantially mitigated for the cells operated with 5 and 20 ppm H_2S, suggesting a preventative effect of sulfur on the loss of electro-catalytic activity.

All sulfur-exposed cells showed a decrease in performance upon removal of hydrogen sulfide from the feed gas (Figure 6a,b), which reflected in a strong increase of the polarization resistance in the frequency range from 0.1 to 10 Hz in the first 5 h, as demonstrated for the cell exposed to 20 ppm H_2S in Figure 7a,b. This resistance increase was larger than the initial sulfur-induced resistance decrease, indicating the onset of further degradation after sulfur removal, which is confirmed by a further increase in degradation rate as shown in Figure 6a,b. For the cell exposed to 20 ppm H_2S, the impedance spectra showed a significant increase of both ohmic and polarization resistance in the time period between 600 and 644 h, which was higher than their degradation in the previous 600 h. Because of the higher degradation rate after sulfur removal, the total degradation of the cells exposed to sulfur was higher than that of the sulfur-free cells when the degradation after sulfur removal was included.

2.5. Post-Test Analysis

Polished SEM images of both samples in **Figure 8**a,b showed significant microstructural changes compared to the initial structure (Figure 4a), notably the formation of blurred regions where the initial pores were clogged. The SEM/energy dispersive X-ray spectroscopy (EDX) mappings (Figure 8c,d) show a homogeneous distribution of Ce within both electrodes, whereas the elements Sr, Fe, and Mo are heterogeneously distributed. A reduced EDX intensity for Fe and Mo was observed within 5 µm of the Pt

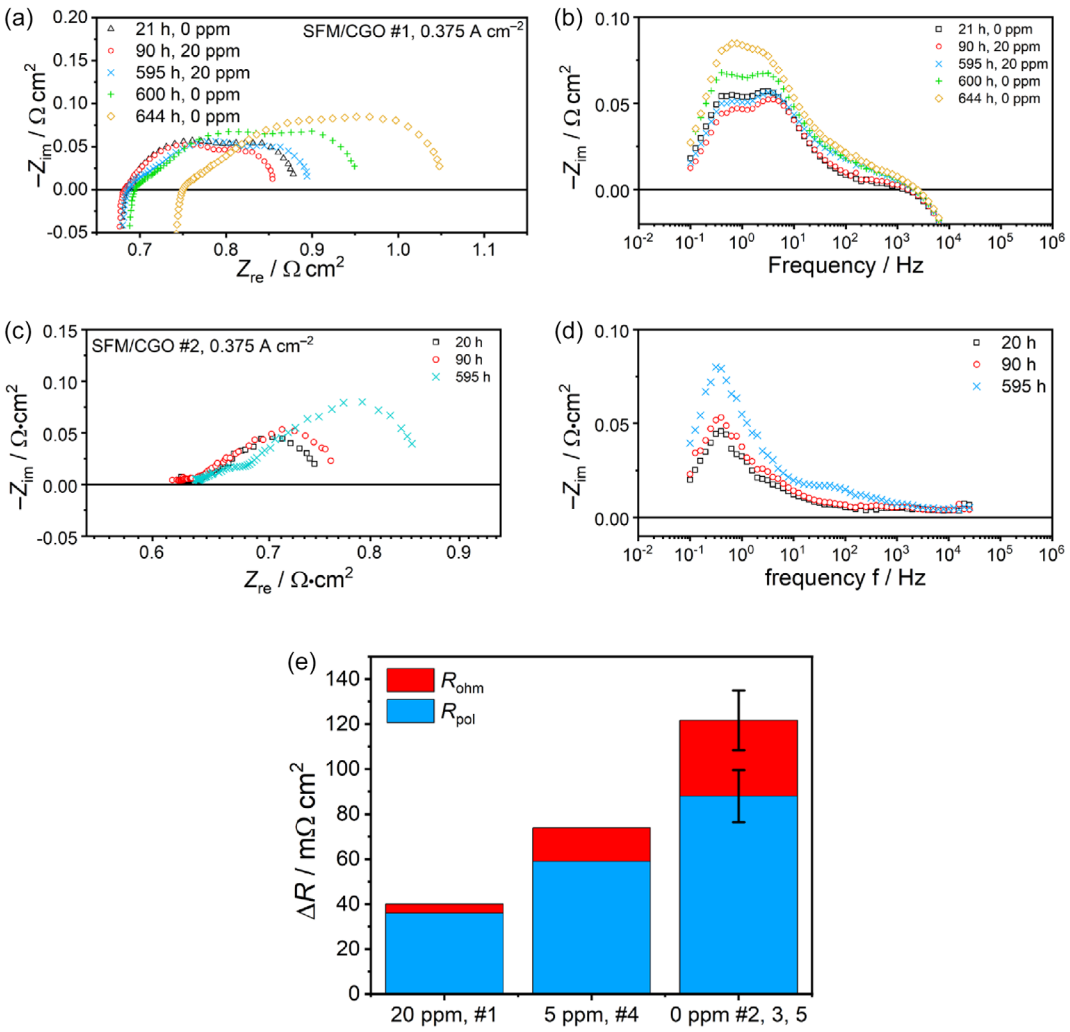

Figure 7. a) Nyquist and b) imaginary impedance plots of the SFM/CGO #1 cell over time with exposure to 20 ppm H_2S. c) Nyquist and d) imaginary impedance plots of the SFM/CGO #1 cell over time without exposure to H_2S. e) Change of ohmic and polarization resistance during 500 h durability testing for the cells exposed to 20 and 5 ppm H_2S. Average and standard deviation values were calculated for the cells not exposed to sulfur. Malfunctioning of the testing hardware in the case of the 1 ppm H_2S prevented the recording of EIS data.

current collector in both electrodes (see additional mapping images in Figure S9 and S10, Supporting Information). Both Fe and Mo were detected in the Pt current collector in Figure 8c, whereas the Pt layer in Figure 8d was already removed during cell disassembly, preventing detailed analysis. The existence of PtFe and PtMo alloys with up to 20 mol% Fe and Mo, respectively, at 800 °C has been reported.[47,48] However, a ternary alloy combining all three metals is not yet well-documented.

Strontium segregations were detected in the outermost parts of both fuel electrodes with no overlap of either Fe or Mo, and similar segregations were observed in the CGO interlayers. This behavior indicates the demixing of the SFM phase and high elemental mobility within the electrode. Since the SFM decomposition reactions, as given in Equation (1) and (2), are less favorable at low hydrogen partial pressures, decomposition is expected to be less pronounced close to the electrode/electrolyte interface where pH_2 is lowest. By contrast, SFM decomposition should be accelerated close to the current collector where pH_2 is highest.

The formed metallic FeMo particles have a high diffusional mobility, which could drive the preferential diffusion of Fe and Mo away from the current collector toward regions where they stabilize in different forms, such as R–P phases.

One plausible mechanism for the Sr redistribution in the electrode could be the formation of volatile $Sr(OH)_2$A similar mechanism has been proposed for LSCF oxygen electrodes in wet air.[49] In LSCF, SrO first segregates and then reacts with steam to form $Sr(OH)_2$ according to

$$SrO + H_2O \rightleftharpoons Sr(OH)_2 \quad (5)$$

SrO surface segregation has also been reported for SFM,[50] and may be further enhanced by the formation of the R–P phases

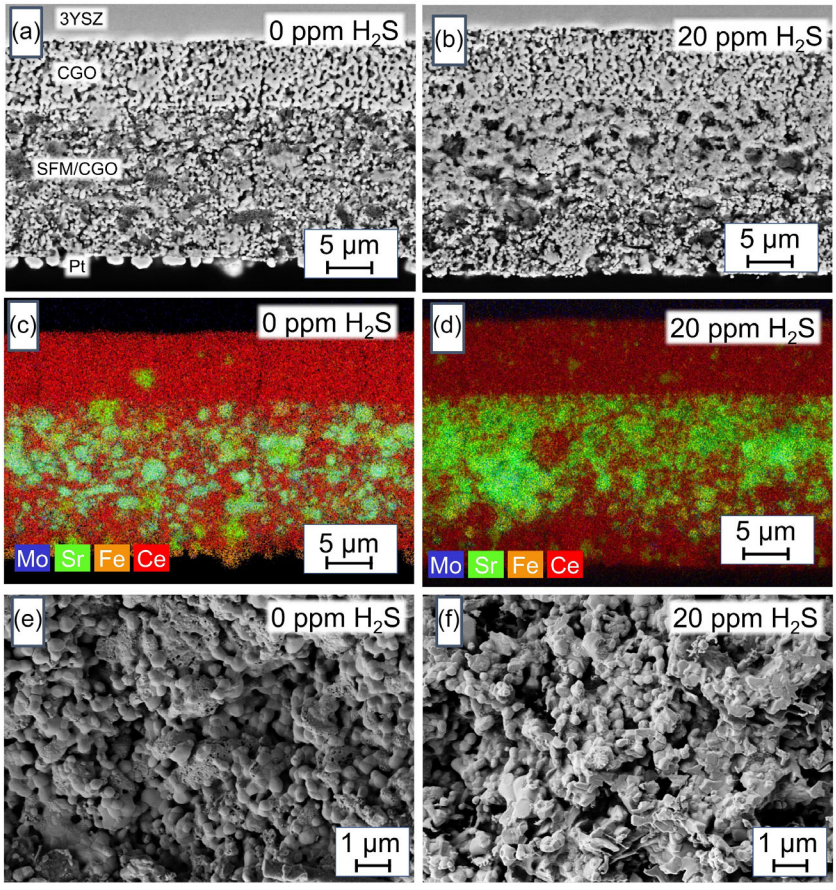

Figure 8. a,b) Polished SEM, c,d) EDX images, and e,f) fracture SEM images of (a,c,e) SFM/CGO #2 and (b,d,f) SFM/CGO #1. The polished SEM/EDX images of the SFM/CGO #2 samples still show the Pt current collector layer, whereas the Pt layer of SFM/CGO #1 was removed after testing.

(Equation 1 and 2) due to excess Sr in these compounds. Kinetics of Equation (1) and (2) are likely faster close to the current collector due to higher pH_2, and hence, the formation of volatile $Sr(OH)_2$ should be favorable if SrO segregation is the rate-limiting step. According to the pH_2O gradient in the electrode, $Sr(OH)_2$ could subsequently be transported out of the electrode into the fuel gas outlet.

Alternatively, Sr could migrate as Sr^{2+} ion within the oxide lattice due to the electric field across the SOFC. The negative charge at the opposing electrode may drive Sr ions away from the current collector toward the electrolyte, where they may stabilize again.

The change in fuel electrode composition led to a further performance loss over time. Since the initial SFM phase was likely responsible for the electronic conductivity of the composite electrode, its depletion in the outer part of the electrodes likely forced a shift in the conduction pathway to the CGO phase, which has lower electronic conductivity. This decrease in effective electrode conductivity likely contributed to an increase in ohmic resistance as it occurred beyond the electrochemically active thickness of the porous electrode, as observed in Figure 7a,c.[43] Additional effective conductivity loss within the electrochemically active part of the electrode would entail an increase in polarization resistance, which was also observed during operation. Thus, a combination of both mechanisms is plausible.

Finally, the fracture SEM images of both electrodes in Figure 8e,f reveal differing degrees of degradation. While the smaller CGO particles still retained a morphology similar to their initial state (see Figure 1a), the SFM particle underwent substantial morphological changes. Pore formation was prominent in the SFM phase of the sulfur-free sample, whereas no such pores could be observed in the sulfur-exposed electrode.

2.6. Mechanistic Discussion

A detailed determination of the hydrogen oxidation mechanism is challenging due to the complex electrochemical behavior, likely influenced by multiple phases, with at least SFM and CGO showing MIEC properties. The electronic conductivity value of CGO under reducing conditions and 800 °C of 0.1–1 S cm^{-1} is comparatively low.[51,52] Since the reported values for SFM are generally between 10 and 45 S cm^{-1},[8,14] SFM is expected to be predominantly responsible for the electronic conductivity in an intact SFM/CGO electrode. However, after the reduction process at 800 °C, the SFM content in the powder mixture was lower than the combined amount of the newly formed R–P phases, Sr_2CeO_4, and Fe. Since the cells did not show an increased ohmic resistance compared to Ni/CGO-based reference cells, it is speculated that the two R–P phases still possess

favorable transport properties, particularly a high electronic conductivity potentially comparable to SFM.

This hypothesis aligns with findings from other literature studies reporting the formation of the R–P structure $Sr_3FeMoO_{7-\delta}$ after in situ reduction of $Sr_2FeMoO_{6-\delta}$ perovskite structures with partial substitution of Mo by Co or Ni.[53,54] For example, in $Sr_2Fe(Mo_{2/3}Co_{1/3})O_{6-\delta}$, the formation of CoFe nanoparticle-decorated Sr_3FeMoO_7 was observed, exhibiting an electrical conductivity of 51 S cm^{-1} at 800 °C.[53] In the present study, the substantial presence of metallic Fe in the fuel electrode after reduction may facilitate hydrogen oxidation since Fe is a good hydrogen dissociation catalyst. However, its extensive interdiffusion within the electrode indicates that Fe particles do not remain anchored in the host perovskite as frequently observed during the "exsolution" process and their formation is generally undesired.

SFM decomposition may not necessarily be harmful initially since the fuel electrodes showed high performance and favorable sulfur activation characteristics. However, after the initial SFM decomposition, the gradual reorganization of the SFM-derived phases was most likely the cause for the observed degradation since it entailed a loss of phase percolation and reduction in the electrochemically active surface area.

The precise mechanism behind the sulfur-enhanced performance and durability of the SFM/CGO electrodes remains unclear. Interestingly, a 10% performance drop was observed after sulfur poisoning of an SFM electrode with 100 ppm H_2S at 800 °C in another study.[28] Furthermore, decomposition of SFM was reported after exposure to 800 ppm H_2S.[12] These differences may be due to the differences in hydrogen sulfide concentration. Walker et al. investigated the interactions between SFM and H_2S by density functional theory (DFT) and ab initio thermodynamic analysis, finding that oxygen replacement by sulfur on the SFM surface was energetically more favorable than H_2S dissociative adsorption.[30] They predicted that neither process would occur below 100 ppm H_2S, and emphasized that surface termination strongly influences sulfur incorporation. Although the present study operated well below 100 ppm H_2S, the observed impact on the ohmic resistance suggests a change in the bulk properties of SFM, potentially involving oxygen substitution by sulfur. This incorporation of sulfur in SFM and the R–P phases may enhance transport properties and surface ion exchange rate, possibly by controlling oxygen vacancy formation or improving oxygen ion mobility. Such substitution could help to maintain an optimal oxygen vacancy concentration, preventing vacancy over-formation that can decrease ionic conductivity due to vacancy clustering.[55] Furthermore, sulfur-induced lattice strain might increase ionic conductivity.[56] Excessive oxygen vacancy formation can also lead to significant lattice distortions and destabilize the crystal structure of a perovskite, eventually resulting in the observed structural decomposition. After switching off the hydrogen sulfide supply, the removal of sulfur from the perovskite/R–P lattice would lead to an immediate loss of its stabilizing effects and possibly enhanced oxygen vacancy formation, clustering, and exacerbated decomposition. It is acknowledged that the proposed effect of sulfur is hypothetical, as no direct mechanistic evidence is provided in this work. Detailed mechanistic studies would ideally require operando investigations of SFM/CGO fuel electrodes exposed to sulfur, which involve significant experimental effort. Ex situ investigations are also limited, as sulfur is removed during cooling in a forming gas atmosphere for safety, and compositional changes during cooling prevent reliable mechanistic insight.[57]

3. Conclusions

Nickel-free, perovskite-based SFM/CGO fuel electrodes were successfully integrated into $5 \times 5\ cm^2$ electrolyte-supported SOFCs, enabling direct benchmarking against state-of-the-art Ni/CGO electrodes using an identical cell architecture. With H_2/H_2O fuel gas at 800 °C, the SFM/CGO cells showed slightly lower performance. No difference in ohmic resistance between the two cell types was observed, suggesting that electronic conductivity and current collection in the perovskite fuel electrode were not limiting factors. However, higher polarization resistances indicated reduced electro-catalytic activity.

Remarkably, the addition of trace H_2S to the fuel enhanced both performance and electrochemical stability of the SFM/CGO electrodes, in stark contrast to the typical degradation behavior of Ni/cermet fuel electrodes. This effect manifested as a reduction in polarization resistance and slower performance decrease over time, suggesting a unique sulfur-induced stabilization mechanism. Nevertheless, the underlying mechanism remains to be fully elucidated and could be further investigated using operando electrochemical and spectroscopic techniques. Despite this improvement, long-term durability tests revealed that SFM remains structurally unstable in hydrogen-rich atmospheres at 800 °C. Post-test analysis confirmed phase decomposition and microstructural reorganization. Interestingly, the newly formed secondary phases exhibited unexpectedly high electrochemical activity, opening new opportunities for exploring alternative phase-stabilized compositions.

In summary, while SFM/CGO composites show promise as Ni-free fuel electrodes with unusual sulfur-enhanced performance, their limited structural stability under standard SOFC conditions currently hinders commercial viability. Overall, this study introduces sulfur as a potential tool for stabilizing complex oxides under harsh conditions. Future research should focus on doping strategies or lower operating temperatures to enhance long-term stability and unlock the full potential of this class of materials for next-generation sulfur-tolerant SOFCs.

4. Experimental Section

Powder Characterization: SFM powder supplied by Marion Technologies (Verniolle, France) was calcined at 1300 °C to obtain high crystallinity. The calcined powder was ground with a planetary ball-mill to breakdown the particles. $Ce_{0.9}Gd_{0.1}O_{2-\delta}$ (CGO10) powder was supplied by Treibacher (Althofen, Austria). SFM/CGO powder mixtures were obtained by dispersion of mixtures in a 50 vol%/50 vol% ratio in ethanol, roll-milling with ZrO_2 balls and drying at 60 °C. Subsequently, they were sintered at 1100 °C for 1 h to simulate the fuel electrode thermal treatment. Temperature programed reduction (TPR) profiles were recorded using a BELCATII (Microtrac MRB, Japan) on the SFM/CGO mixture. The powder was heated to 150 °C in Ar at 50 ccm and then cooled down below 50 °C prior to the TPR measurement for surface water desorption. The TPR signal was recorded up to 1100 °C with a TCD detector at a temperature increment of 5°K min^{-1} and 5%H_2–Ar gas flow of 50 ccm. Reduced samples were obtained by annealing the powders at the desired

temperatures (450, 600, 670, 740, 800, and 860 °C) in the flow of pure hydrogen for 2 h. The sample powders were analyzed by XRD) using a D8 ADVANCE (BRUKER AXS GmbH, Germany) device with a Cu Kα radiation source operating at 40 kV and 40 mA in Bragg-Brentano geometry to identify the phases and determine their structural parameters. XRD diffractograms were recorded at an increment step of 0.02° using a high-resolution position sensitive detector (LYNXEYE XE-T) operated in 1D high resolution mode with a motorized divergence slit (fixed sample illumination mode: length 12 mm), and 2.5° and 4° axial soller slits were used for incident and receiving X-ray, respectively. Crystalline phases were identified with ICDD database and Rietveld refinement was carried out on the XRD data using TOPAS software. Compositional ratio, lattice parameters, crystallite sizes/strain of the phases were refined. A Chebyshev polynomial model (7th order) was used for back-ground function and sample displacement correction was used in the refinement. A surface roughness correction was applied according to Pitschke et al.[58]

Dilatometry measurements were performed to determine the coefficient of thermal expansion (CTE) value of SFM on DIL 402 C (Netzsch, Germany) in the temperature range of 25–1200 °C at a heating rate of 3 °C min^{-1} in ambient air to investigate the thermal expansion behavior. A dense ceramic rod of SFM was prepared by high temperature sintering for the dilatometry.

Cell Manufacturing: The calcined SFM powder was ball-milled to obtain an appropriate grain size for the electrode. SFM/CGO fuel electrode inks were prepared by dispersing the powders with 50 vol%/50 vol% ratios in a 94 wt% α-Terpineol and 6 wt% ethyl cellulose solution with a powder to solution ratio of 2:1 and mixing in a 3-roll mill. Subsequently, ESCs were manufactured by using a commercial 5×5 cm^2-sized substrate of 90 µm thick 3 mol% Y_2O_3-doped ZrO_2 (3YSZ) electrolytes coated on both sides with 5 µm thick CGO layers from Kerafol GmbH (Eschenbach, Germany). 4×4 cm^2-sized SFM/CGO composites fuel electrodes were applied via screen-printing. The resulting half cells were fired at 1100 °C for 1 h in air with a heating rate of 3 K min^{-1}. Afterward, the oxygen electrode was screen-printed on the other side of the electrolyte with a commercial ink of LSCF supplied by Heraeus GmbH (Hanau, Germany), resulting in an oxygen electrode thickness of ≈25 µm. Pt paste was brushed on the sintered fuel electrode surface for current collection. Then, the cell was fired at 1050 °C for 1 h in air with a heating rate of 3 K min^{-1}. In addition, state-of-the-art cells supplied by Sunfire GmbH (Dresden, Germany), having a similar architecture, were investigated to allow for a comparative assessment of the fuel electrode performances. Therefore, a similar cell architecture was used that also consisted of a CGO (5 µm)|3YSZ (90 µm)|CGO (5 µm) sandwich structure and employed a Ni/CGO fuel electrode and an LSCF/CGO oxygen electrode.

Electrochemical Characterization: The setup for cell testing enables the characterization of up to four cells simultaneously under variation of current density and has been illustrated and described in detail elsewhere.[2] The high reproducibility of measurements between the different positions has been demonstrated in previous studies.[59–61] The cells were heated (3 K min^{-1}) to 800 °C for reduction in pure hydrogen for 2 h prior to the operation. Proper sealing of all cells was ensured by confirming the open circuit voltage (OCV) to be higher than 1.2 V in pure hydrogen and air. Pt and Au meshes were used for contacting on the fuel electrode and the oxygen electrode side, respectively. All cells were operated at 860 °C with 97% H_2 and 3% H_2O at a constant total fuel flow rate of 1 SLPM for every cell. H_2S was taken from a pressurized H_2S/H_2 bottle that contained 200 ppm H_2S. Air was supplied to the oxygen electrode at a constant flow rate of 1 SLPM. EIS was performed by means of an electrochemical workstation (Zahner PP-240 with Thales software) in a frequency range from 20 mHz to 100 kHz with 10 points per decade. The amplitude of the current stimulus was chosen to be 500 mA, which was shown to lie within the linear regime by i–V curves.

Microstructural Characterization: SEM images were acquired using a Zeiss Ultra Plus SEM in combination with a Bruker XFlash 5010 EDX detector for elemental analysis. The elemental distribution across the cross-sectional surfaces of the reference and post-tested samples was investigated using high-resolution secondary ion mass spectrometry imaging analysis apparatus (SIMS, NanoSIMS 50L, Ametek CAMECA). The samples were infiltrated with a high-vacuum-compatible resin, then further embedded into the NanoSIMS-specific sample holder using an alloy of Bi-Sn, and the exposed surfaces were subsequently polished using diamond slurry. Lastly, the samples were coated with evaporated osmium (Os) to improve conductivity. For the SIMS measurements, a Cs+ primary ion beam accelerated at 8 kV was scanned across the sample surfaces (raster areas: 30 µm × 30 µm, 10 µm × 10 µm). Secondary ion mass species of $^{16}O^-$, $^{56}Fe^{16}O^-$, $^{88}Sr^{16}O^-$, $^{94}Zr^{16}O^-$, $^{98}Mo^{16}O^-$, $^{140}Ce^{16}O^-$, and $^{158}Gd^{16}O^-$ were detected simultaneously via a multicollection system. Images of 256 × 256 pixels were acquired with a dwell time setting of 20 ms/pixel, and image processing was performed using WinImage ver. 4.6 software (Ametek, Cameca)

Supporting Information

Supporting Information is available from the Wiley Online Library or from the author.

Acknowledgements

The authors gratefully acknowledge financial support from the German Ministry for Economic Affairs and Energy (BMWi) within the framework of the project "Kostenoptimierter Stack und verbessertes Offgrid-System (KOSOS)" via grant number 03ETB005C and the German Federal Ministry for Research, Technology and Space (BMFTR) "H2Giga–HTEL-Stacks" via grant number 03HY124E.

Open Access funding enabled and organized by Projekt DEAL.

Conflict of Interest

The authors declare no conflict of interest.

Data Availability Statement

The data that support the findings of this study are available in the supplementary material of this article.

Keywords

perovskite, solid oxide cells, solid oxide electrolysis cell, solid oxide fuel cell, sulfur poisoning

Received: October 15, 2025
Revised: December 15, 2025
Published online:

[1] M. Riegraf, V. Yurkiv, G. Schiller, R. Costa, A. Latz, K. A. Friedrich, *J. Electrochem. Soc.* **2015**, *162*.
[2] M. Riegraf, M. P. Hoerlein, R. Costa, G. Schiller, K. A. Friedrich, *ACS Catal.* **2017**, *7*, 7760.
[3] M. Riegraf, V. Yurkiv, R. Costa, G. Schiller, K. A. Friedrich, *ChemSusChem* **2017**, *10*, 587.
[4] J. Mermelstein, M. Millan, N. Brandon, *J. Power Sources* **2010**, *195*, 1657.
[5] V. Yurkiv, A. Latz, W. G. Bessler, *ECS Trans.* **2013**, *57*, 2637.
[6] B. Iwanschitz, J. Sfeir, A. Mai, M. Schütze, *J. Electrochem. Soc.* **2009**, *157*, B269.
[7] L. Shu, J. Sunarso, S. S. Hashim, J. Mao, W. Zhou, F. Liang, *Int. J. Hydrogen Energy* **2019**, *44*, 31275.

[8] L. Skutina, E. Filonova, D. Medvedev, A. Maignan, *Materials* **2021**, *14*, 1715.
[9] G. Miao, C. Yuan, T. Chen, Y. Zhou, W. Zhan, S. Wang, *Int. J. Hydrogen Energy* **2016**, *41*, 1104.
[10] J. Rager, M. Zipperle, A. Sharma, J. MacManus-Driscoll, *J. Am. Ceram. Soc.* **2004**, *87*, 1330.
[11] L. dos Santos-Gómez, L. León-Reina, J. Porras-Vázquez, E. Losilla, D. Marrero-López, *Solid State Ionics* **2013**, *239*, 1.
[12] K. Zheng, K. Świerczek, J. M. Polfus, M. F. Sunding, M. Pishahang, T. Norby, *J. Electrochem. Soc.* **2015**, *162*, F1078.
[13] Q. Liu, X. Dong, G. Xiao, F. Zhao, F. Chen, *Adv. Mater.* **2010**, *22*, 5478.
[14] D. Osinkin, *J. Power Sources* **2019**, *418*, 17.
[15] B. He, L. Zhao, S. Song, T. Liu, F. Chen, C. Xia, *J. Electrochem. Soc.* **2012**, *159*, B619.
[16] G. Xiao, Q. Liu, F. Zhao, L. Zhang, C. Xia, F. Chen, *J. Electrochem. Soc.* **2011**, *158*, B455.
[17] D. Osinkin, N. Lobachevskaya, A. Kuz'min, *Russ. J. Appl. Chem.* **2017**, *90*, 41.
[18] C. Zhu, S. Hou, X. Hu, J. Lu, F. Chen, K. Xie, *Nat. Commun.* **2019**, *10*, 1.
[19] K. P. Ramaiyan, L. H. Denoyer, A. Benavidez, F. H. Garzon, *Commun. Chem.* **2021**, *4*, 139.
[20] L. Bernadet, C. Moncasi, M. Torrell, A. Tarancón, *Int. J. Hydrogen Energy* **2020**, *45*, 14208.
[21] D. A. Osinkin, A. V. Khodimchuk, N. M. Porotnikova, N. M. Bogdanovich, A. V. Fetisov, M. V. Ananyev, *Energies* **2020**, *13*, 250.
[22] S. Suthirakun, S. C. Ammal, A. B. Muñoz-García, G. Xiao, F. Chen, H.-C. zur Loye, E. A. Carter, A. Heyden, *J. Am. Chem. Soc.* **2014**, *136*, 8374.
[23] D. A. Osinkin, *Electrochim. Acta* **2021**, *389*, 138792.
[24] Y. Guo, T. Guo, S. Zhou, Y. Wu, H. Chen, X. Ou, Y. Ling, *Ceram. Int.* **2019**, *45*, 10969.
[25] N. Dai, Z. Lou, Z. Wang, X. Liu, Y. Yan, J. Qiao, T. Jiang, K. Sun, *J. Power Sources* **2013**, *243*, 766.
[26] Y. Wang, T. Liu, S. Fang, F. Chen, *J. Power Sources* **2016**, *305*, 240.
[27] C. Xu, L. Zhang, W. Sun, R. Ren, X. Yang, M. Ma, J. Qiao, Z. Wang, S. Zhen, K. Sun, *J. Mater. Chem. A* **2022**, *10*, 16280.
[28] Q. Liu, D. E. Bugaris, G. Xiao, M. Chmara, S. Ma, H.-C. zur Loye, M. D. Amiridis, F. Chen, *J. Power Sources* **2011**, *196*, 9148.
[29] E. Union, *Off. J. Eur. Union* **2009**, *5*, 2009.
[30] E. Walker, S. C. Ammal, S. Suthirakun, F. Chen, G. A. Terejanu, A. Heyden, *J. Phys. Chem. C* **2014**, *118*, 23545.
[31] J. Feng, G. Yang, N. Dai, Z. Wang, W. Sun, D. Rooney, J. Qiao, K. Sun, *J. Mater. Chem. A* **2014**, *2*, 17628.
[32] M. Florea, F. Matei-Rutkovska, G. Postole, A. Urda, F. Neatu, V. Pârvulescu, P. Gelin, *Catal. Today* **2018**, *306*, 166.
[33] A. F. a. Guillermet, *Bull. Alloy Phase Diagr.* **1982**, *3*, 359.
[34] H. Li, Y. Tian, Z. Wang, F. Qie, Y. Li, *RSC Adv.* **2012**, *2*, 3857.
[35] Z. Wang, Y. Tian, Y. Li, *J. Power Sources* **2011**, *196*, 6104.
[36] M. Gou, R. Ren, W. Sun, C. Xu, X. Meng, Z. Wang, J. Qiao, K. Sun, *Ceram. Int.* **2019**, *45*, 15696.
[37] G. Xiao, Q. Liu, S. Wang, V. G. Komvokis, M. D. Amiridis, A. Heyden, S. Ma, F. Chen, *J. Power Sources* **2012**, *202*, 63.
[38] M. Santaya, L. Toscani, L. Baqué, H. E. Troiani, L. Mogni, *Solid State Ionics* **2019**, *342*, 115064.
[39] X. Pan, Z. Wang, B. He, S. Wang, X. Wu, C. Xia, *Int. J. Hydrogen Energy* **2013**, *38*, 4108.
[40] N. Dai, J. Feng, Z. Wang, T. Jiang, W. Sun, J. Qiao, K. Sun, *J. Mater. Chem. A* **2013**, *1*, 14147.
[41] F. Tietz, *Ionics* **1999**, *5*, 129.
[42] M. Riegraf, K. Develos-Bagarinao, I. Biswas, R. Costa, *J. Power Sources* **2023**, *559*, 232669.
[43] M. Riegraf, D.-M. Amaya-Dueñas, N. Sata, K. A. Friedrich, R. Costa, *ChemSusChem* **2021**, *14*, 1.
[44] C. Grosselindemann, N. Russner, S. Dierickx, F. Wankmüller, A. Weber, *J. Electrochem. Soc.* **2021**, *168*, 124506.
[45] S. B. Adler, J. A. Lane, B. C. H. Steele, *J. Electrochem. Soc.* **1996**, *143*, 3554.
[46] J. Fleig, *Phys. Chem. Chem. Phys.* **2005**, *7*, 2027.
[47] Y. Nosé, A. Kushida, T. Ikeda, H. Nakajima, K. Tanaka, H. Numakura, *Mater. Trans.* **2003**, *44*, 2723.
[48] L. Brewer, R. H. Lamoreaux, R. Ferro, R. Marazza, *Bull. Alloy Phase Diagr.* **1980**, *1*, 89.
[49] X. Yin, L. Bencze, V. Motalov, R. Spatschek, L. Singheiser, *Int. J. Appl. Ceram. Technol.* **2018**, *15*, 380.
[50] H.-Y. Li, P.-C. Su, *Appl. Mater. Today* **2023**, *31*, 101769.
[51] Y.-P. Xiong, H. Kishimoto, K. Yamaji, M. Yoshinaga, T. Horita, M. E. Brito, H. Yokokawa, *Solid State Ionics* **2011**, *192*, 476.
[52] M. Mogensen, T. Lindegaard, U. R. Hansen, G. Mogensen, *J. Electrochem. Soc.* **1994**, *141*, 2122.
[53] X. Xi, Z.-S. Cao, X.-Q. Shen, Y. Lu, J. Li, J.-L. Luo, X.-Z. Fu, *J. Power Sources* **2020**, *459*, 228071.
[54] Z. Du, H. Zhao, S. Yi, Q. Xia, Y. Gong, Y. Zhang, X. Cheng, Y. Li, L. Gu, K. Świerczek, *ACS Nano* **2016**, *10*, 8660.
[55] D. Y. Wang, D. S. Park, J. Griffith, A. S. Nowick, *Solid State Ionics* **1981**, *2*, 95.
[56] G. F. Harrington, L. Sun, B. Yildiz, K. Sasaki, N. H. Perry, H. L. Tuller, *Acta Mater.* **2019**, *166*, 447.
[57] Z. Cheng, J. H. Wang, Y. Choi, L. Yang, M. C. Lin, M. Liu, *Energy Environ. Sci.* **2011**, *4*, 4380.
[58] W. Pitschke, H. Hermann, N. Mattern, *Powder Diffr.* **1993**, *8*, 74.
[59] M. P. Hoerlein, M. Riegraf, R. Costa, G. Schiller, K. A. Friedrich, *Electrochim. Acta* **2018**, *276*, 162.
[60] M. Riegraf, F. Han, N. Sata, R. Costa, *ACS Appl. Mater. Interfaces* **2021**, *13*, 37239.
[61] M. Riegraf, A. Zekri, M. Knipper, R. Costa, G. Schiller, K. A. Friedrich, *J. Power Sources* **2018**, *380*, 26.